Phase mixing and echoes in a pure electron plasma[a)]

J. H. Yu,[b)] C. F. Driscoll, and T. M. O'Neil
Department of Mechanical and Aerospace Engineering, University of California at San Diego, La Jolla, California 92093 and Physics Department and Institute for Pure and Applied Physical Sciences, University of California at San Diego, La Jolla, California 92093

The two-dimensional (2D) fluid echo is a spontaneous appearance of a diocotron wave after two externally excited waves have damped away, explicitly demonstrating the reversible nature of spatial Landau damping. The inviscid damping, or phase mixing, is directly imaged by a low-noise charge-coupled device camera, which shows the spiral wind-up of the density perturbation. Surprisingly, the basic echo characteristics agree with a simple nonlinear ballistic theory that neglects all collective (i.e., mode) effects. Also, the simple 2D picture is violated by end confinement fields that cause v_z-dependent θ drifts, so the observed echo must be interpreted as a superposition of separately damping and separately echoing velocity classes. The maximal echo lifetimes agree with a theory describing weak collisional velocity scattering between velocity classes. In addition, large second wave excitations degrade the echo up to 5× faster than collisions. © *2005 American Institute of Physics.* [DOI: 10.1063/1.1885006]

I. INTRODUCTION

Echo phenomena have been seen in a variety of systems spanning many scientific disciplines, including optics,[1] atomic physics,[2] and plasma physics.[3–5] In general, echoes involve the dissipationless phase mixing of a macroscopic signal. Later in time, a second excitation is applied and this perturbation also damps. The echo is the "spontaneous" appearance of a macroscopic signal long after the two external excitations damp away, and provides an explicit demonstration that the phase mixing is thermodynamically reversible.

Here, experimental measurements of two-dimensional (2D) fluid echoes are presented, demonstrating the reversible nature of spatial Landau damping. Fluid echoes have been predicted theoretically[6,7] and studied numerically,[8] but viscosity or other nonideal effects have prevented echo observations in conventional fluids. We use a magnetized electron column as the "working fluid" to study the echo; the z-averaged $\mathbf{E} \times \mathbf{B}$ drift dynamics of the electron column is isomorphic to the 2D (r, θ) dynamics of an ideal (incompressible and inviscid) fluid.[9] Thus, the echoes represent Kelvin wave[10] echoes, that is, surface wave echoes on a 2D inviscid vortex.

We demonstrate that the echo mode number, echo appearance time, and nonlinear saturation effect agree with a simple nonlinear ballistic theory. In addition, we find that the maximal echo lifetime is fundamentally limited by electron-electron collisions, but can also be limited by large amplitude effects.

To produce the echo, we first launch a surface drift wave on a quiescent electron column with density $n_0(r)$. These "diocotron waves"[11] have density perturbation $\delta n_i(r)e^{i(m_i\theta - \omega_i t)}$ with $m_i = 2, 3, 4, \ldots$, and are essentially uni-

form in z. The measured wave electric field at the cylindrical wall is proportional to the radial integral over δn. For our chosen profiles $n(r)$, the excited wave rapidly damps away by the phase mixing of spatial Landau damping:[12] strong radial shear in the $\mathbf{E} \times \mathbf{B}$ rotation frequency $\omega_E(r)$ causes progressive spiral wind-up of the perturbation $\delta n_i(r, \theta, t)$ near the critical radius r_c, where the wave-particle resonance $\omega_E(r_c) = \omega_i/m_i$ is satisfied. Essentially, each "shell" of the plasma rotates at a different rate, stretching the initially aligned (θ localized) density perturbation into a spiral. The perturbed density then becomes a rapidly oscillating function of r, so the wave potential $\delta\phi$ phase mixes to zero. Although the wave potential vanishes, the spiral phase-mixing pattern remains stored in $\delta n_i(r, \theta, t)$.

After a chosen time τ, a second diocotron wave is launched and it too damps away, leaving its own phase-mixing pattern $\delta n_s(r, \theta, t)$. The second wave excitation also modulates the perturbation remaining from the first wave, producing a second-order perturbation $\delta n^{(2)}(r, \theta, t)$. This second-order perturbation begins to unmix, and after some time the perturbations in the various shells realign, producing a wave electric field which is the echo.

A simple representation of spiral wind-up and echo formation is shown in Fig. 1, using initial azimuthal mode number $m_i = 2$ and second mode number $m_s = 4$. Here, white represents positive $\delta n(r, \theta, t)$, black represents negative $\delta n(r, \theta, t)$, and δn is treated as a passive tracer density field that is advected by the sheared $\mathbf{E} \times \mathbf{B}$ flow. The essential feature of the second excitation is to produce radial drifts of particles, shown in Fig. 1(d). The modulated spiral pattern evolves with the shear flow $\omega_E(r)$, and after some time begins to unwind. At time $t = 2\tau$, the perturbation forms an $m_e = 2$ echo, shown in Fig. 1(f).

This simple description of the 2D echo is complicated by 3D "end" effects that make ω_E dependent on an electron's z velocity, i.e., $\omega_E(r, v_z)$.[13] That is, energetic electrons pen-
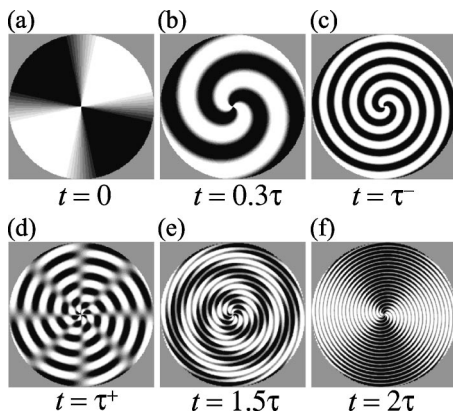

FIG. 1. Simple representation of phase mixing and unmixing, using (a) m_i =2 and (d) m_s=4, resulting in (f) m_e=2.

FIG. 2. Electron trap with CCD camera density diagnostic. The wall signal from sectored electrodes is used to measure the wave amplitudes.

etrate further into the end confinement potential, and therefore have a different z-averaged $\omega_E(r,v_z)$. Different z-velocity classes must *separately* phase mix and unmix to form a combined echo, so it is somewhat surprising that the echo occurs at all (because these 3D end effects lie outside the 2D fluid perspective). We will see that collisional velocity scatterings between velocity classes fundamentally limit this recombination.

The fluid echoes are closely related to plasma wave echoes.[4,5] Indeed, the description of a plasma wave echo differs from the above 2D description only in that the wave electric field is given by an integral over the perturbation in the phase-space distribution $\delta f(z,p_z,t)$. The Landau damping of $k_z \neq 0$ plasma waves is a phase-mixing process where $\delta f(z,p_z,t)$ becomes progressively more rapidly oscillating in p_z, and the integral vanishes. However, a phase-mixing pattern remains stored in $\delta f(z,p_z,t)$, and this produces an echo when it unmixes after modulation by a second wave.

The spatial Landau damping of fluid echoes is a wave-particle resonance that occurs in configuration space as opposed to the resonance in velocity space for longitudinal plasma waves. Indeed, phase space (θ,p_θ) is equivalent to configuration space (θ,r^2) in a strongly magnetized electron column, because the angular momentum in $\mathbf{E}\times\mathbf{B}$ drift dy-
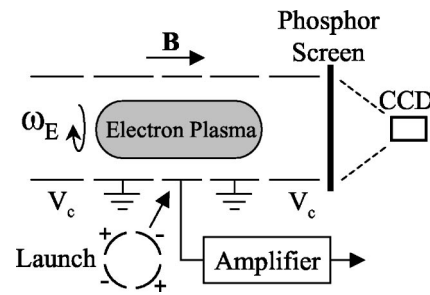
namics is given by $p_\theta=(eB/2c)r^2$.[12] Thus, the phase mixing and unmixing are observed directly in measurements of $n(r,\theta,t)$.

II. EXPERIMENTAL SETUP

The experiments are performed on a magnetized pure electron plasma confined in a Penning–Malmberg trap, shown in Fig. 2. A hot tungsten source injects electrons into a stack of cylindrical electrodes. The electrons are trapped axially by voltages $-V_c=-100$ V applied to end cylinders; the strong axial magnetic field (0.2 kG$\leq B \leq$7 kG) provides radial confinement, and causes rapid cyclotron motion at frequency Ω_c. The vacuum chamber (with neutral gas pressure $P \lesssim 10^{-10}$ torr) resides inside the bore of the superconducting solenoid.

The plasma typically has a central density $n_o \approx 1 \times 10^7$ cm^{-3}, with a length varied over the range $5 \leq L_p \leq 70$ cm inside a wall radius $R_w=3.5$ cm. We adjust the plasma radius to $R_p \approx 1.5$ cm, and create a broad radial tail to produce strong damping, as shown in Fig. 3.

The electrons have thermal energy $4 \leq T \leq 10$ eV, giving an axial bounce frequency $f_b \equiv \bar{v}/2L_p \approx (0.5$ MHz$)T^{1/2}(L_p/50)^{-1}$ and a Debye shielding length $\lambda_D \approx (0.25$ cm$)T^{1/2}(n/10^7)^{-1/2}$. Here, the thermal velocity is $\bar{v} \equiv \sqrt{T/M}$. The electron space charge creates a central potential $-\phi_p \approx -30$ V, and the radial electric field causes $\mathbf{E}\times\mathbf{B}$ rotation at a rate $f_E(r) \equiv cE(r)/2\pi rB \approx (150$ kHz$)(n/10^7)$
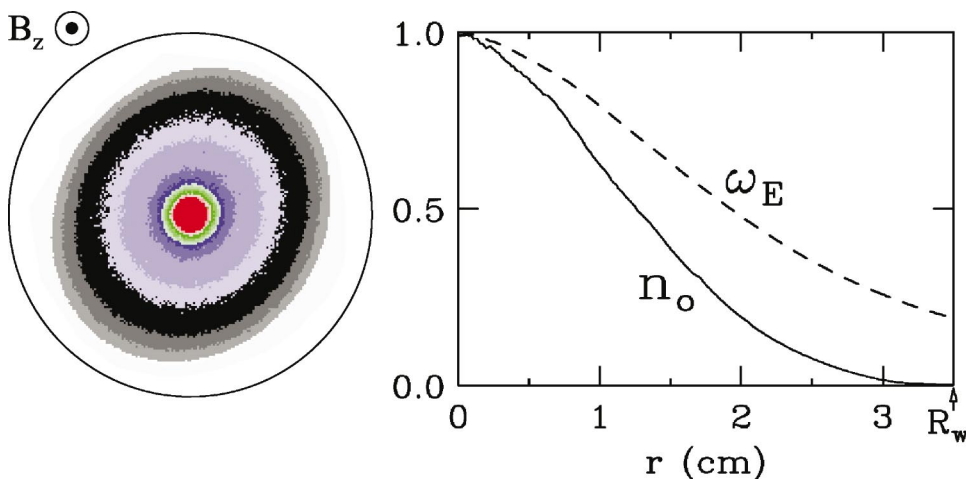

FIG. 3. (Color). CCD image of $m=2$ surface drift wave. Typical density $n_o(r)$ and rotation frequency $\omega_E(r)$ profiles are also shown.
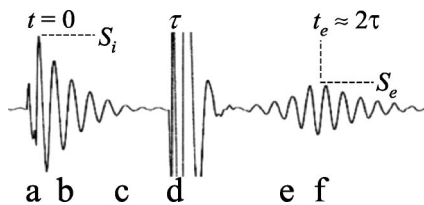
FIG. 4. Measured wall signal showing initial, second, and echo waves.

$\times (B/1\text{ kG})^{-1}$. Later, in Sec. V, we consider 3D end effects that make the rotation frequency depend slightly on v_z.

The frequency ordering is thus

$$\Omega_c/2\pi \gg f_b > f_E, f_m, \tag{1}$$

where $\Omega_c \equiv eB/mc$ is the cyclotron frequency, and f_m is the frequency of the diocotron mode with azimuthal mode m. The fast cyclotron motion makes guiding-center theories applicable, and the fast bounce motion compared with the $\mathbf{E} \times \mathbf{B}$ drift frequency makes the system approximately 2D.

Sectored wall cylinders are used to excite and detect waves in the plasma. A single wall sector can be used as a receiver, or sectors can be used in combination to maximize the signal from a wave with a particular mode number m.

At a chosen time in the evolution, the z-integrated electron density $n(r,\theta,t)$ can be measured by dumping the plasma onto a phosphor screen (biased to 15 kV), imaged by a low-noise 512×512 charge-coupled device (CCD) camera. The shot-to-shot reproducibility is good $[\delta n(r)/n \approx 0.1\%]$, so a time evolution is obtained by creating a sequence of plasmas with identical wave excitations, each dumped at differing times t.

Figure 3 shows an image of a dumped plasma with a $m=2$ diocotron perturbation; the density $n(r,\theta)$ is represented logarithmically by the colors. Here, the amplitude of the surface wave (measured by the eccentricity of the density distribution) is $\sim 100\times$ larger than the perturbations used in echo experiments. A typical density $n_o(r)=\langle n_o(r,\theta)\rangle$ and calculated rotation frequency $\omega_E(r)$ is shown in the box.

III. ECHO IMAGES

At $t=0$ an initial wave, with $m_i=2$ and $\omega_i=2\pi \times 20$ kHz, is excited by applying a voltage $V_i=0.2-10$ V to two 180°-opposed wall sectors for a time $\Delta t_i \sim \pi/\omega_i$. Figure 4 shows the received wall signal as the wave damps away (a–c). The corresponding 2D density is initially "circular," i.e., $n_0(r)$ but it is distorted into an elliptical $n(r,\theta)$ by the initial excitation. The peak received initial and echo wall signals are denoted S_i and S_e, respectively.

The "perturbation" images of Fig. 5 have the symmetric equilibrium subtracted out, displaying $\delta n(r,\theta,t) \equiv n(r,\theta,t) - n_o(r)$, where $n_o(r)$ is the profile obtained at $t=0$ with no wall excitation. The colors show magnitude of δn; the initial amplitude is $|\delta n| \approx 10^{-2} n(r)$ but the color scale is adjusted from image to image to maximize the visibility. The elliptical distortion rotates counterclockwise at frequency ω_i but in ~ 5 wave periods it damps back to a circular cross section due to spatial Landau damping, with spiral wind-up of the density perturbation.

At time τ, a second wave with $m_s=4$ is excited by applying a voltage $V_s=0.2-10$ V to four sectors for $\Delta t_s \sim \pi/\omega_s$. (The visible wall signal represents a spurious coupling of the $m_s=4$ excitation into the $m=2$ detection elec-
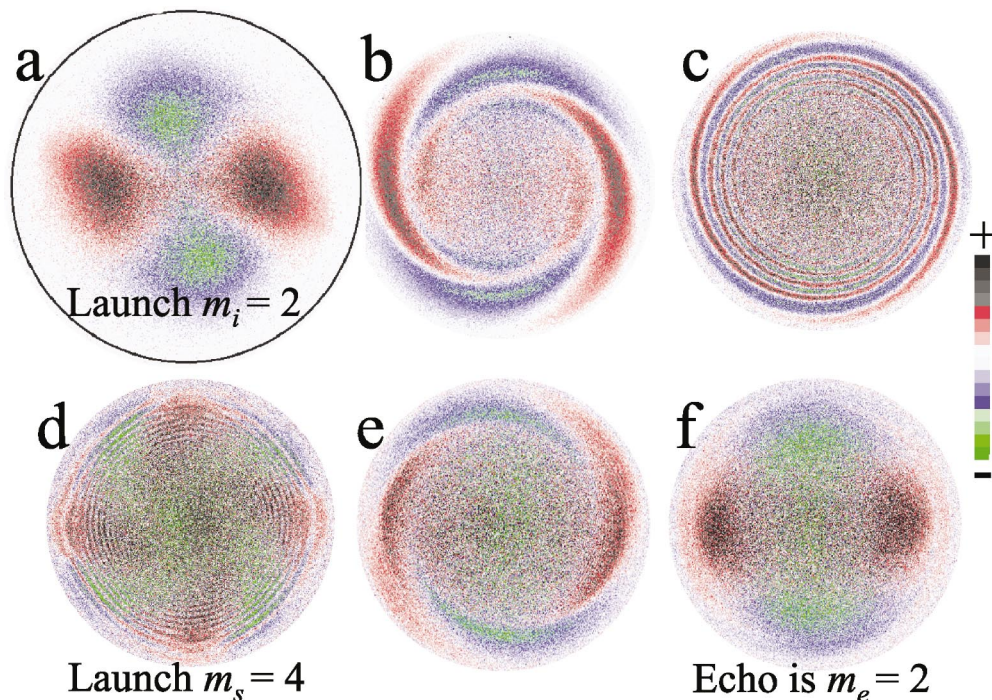

FIG. 5. (Color). Experimental density perturbation images at six successive times. The initial wave is excited in (a) and the density perturbation executes spiral wind-up as the wave is spatially Landau damped. (d) shows the second wave excitation and the echo peaks in (f).

tronics.) The remnants of the phase-mixed initial wave are visible as thin filaments in (d). The second wave excitation causes θ-dependent radial shifts of the filaments; thus, the filaments $\mathbf{E} \times \mathbf{B}$ rotate at a new rate because $\omega_E(r)$ depends on r.

The third wave packet visible in Fig. 4 is the received $m_e = 2$ echo. The initial wave damping effectively unmixed, producing an $m_e = 2$ echo response. The peak echo wall signal S_e occurs at a time $t \approx 2\tau$ for the mode numbers used here. The corresponding image (f) shows $|\delta n| \approx (0.3 \times 10^{-2})n(r)$.

IV. COLLISIONLESS BALLISTIC THEORY

Surprisingly, the essential features of the echo are captured by a collisionless, ballistic theory[4] that completely neglects collective effects such as waves. We solve for the free-streaming $\mathbf{E} \times \mathbf{B}$ drift trajectories of particles, and assume that particle-guiding centers deviate from circular orbits only due to the impulsively applied wall excitation voltages. This ballistic approach is equivalent to treating the particles as passive tracers that orbit at rate $\omega_E(r)$; that is, we assume the perturbed density does not modify the $\mathbf{E} \times \mathbf{B}$ flow.

Here, we calculate the electric field E_w at the wall of the electron trap. The mth Fourier component of the electric potential is

$$\delta\phi_m(r,t) = -e \int_0^{R_w} r'\,dr' \int_0^{2\pi} d\theta'\, n(r',\theta',t) G_m(r|r') e^{-im\theta'},$$

(2)

where (r', θ') is the source point and $G_m(r|r')$ is the Green function.[14]

Following Ref. 4, we use conservation of particles

$$r'\,dr'\,d\theta'\, n(r',\theta',t) = r_o\,dr_o\,d\theta_o\, n_o(r_o)$$

(3)

to express the particle trajectories in terms of the initial ($t=0$) coordinates (r_o, θ_o) and unperturbed density $n_o(r_o)$. The electric field at the wall is then

$$E_w \equiv -\left.\frac{\partial \delta\phi_m(r)}{\partial r}\right|_{R_w}$$

$$= e \int_0^{R_w} r_o\,dr_o \int_0^{2\pi} d\theta_o\, n_o(r_o) g_m[r|r'(r_o,\theta_o,t)] e^{-im\theta(r_o,\theta_o,t)},$$

(4)

where we drop the prime on θ for notational convenience and the radial derivative of the Green function, evaluated at $r=R_w$, is

$$g_m(r|r') \equiv \left.\frac{\partial G_m(r|r')}{\partial r}\right|_{R_w} = \frac{r^m}{R_w^{m+1}}.$$

(5)

Below, we solve for the particle trajectories described by $\theta(r_o, \theta_o, t)$ in the exponential argument of Eq. (4).

The Hamiltonian for 2D $\mathbf{E} \times \mathbf{B}$ drift dynamics is given by

$$H = -e\phi_o(r) + \delta H,$$

(6)

where $\phi_o(r)$ is the unperturbed plasma potential. In general, the perturbed Hamiltonian δH would include self-consistent plasma effects; these effects are ignored in this ballistic approximation. The perturbed Hamiltonian models vacuum potentials created by wall voltages V_i and V_s, applied impulsively at $t=0$ and $t=\tau$,

$$\delta H = eA_i(r)\sin(m_i\theta)\delta(t) - eA_s(r)\sin(m_s\theta)\delta(t-\tau),$$

(7)

where $A_i(r) \equiv a_i V_i \Delta t_i (r/R_w)^{m_i}$, $A_s(r) \equiv a_s V_s \Delta t_s (r/R_w)^{m_s}$ represent the r dependence of the vacuum potentials from the initial and second excitations, and Δt_i, Δt_s represent the actual durations of the applied wall voltages. Here (a_i, a_s) relate the voltages applied on wall sectors to the (m_i, m_s) spatial Fourier components.

The equations of motion follow from Eqs. (6) and (7):

$$\frac{\partial\theta}{\partial t} \equiv \frac{\partial H}{\partial p_\theta} = \frac{c}{eBr}\frac{\partial H}{\partial r} = \omega_E(r) + \frac{c}{Br}\left[\frac{\partial A_i}{\partial r}\sin(m_i\theta)\delta(t)\right.$$

$$\left. + \frac{\partial A_s}{\partial r}\sin(m_s\theta)\delta(t-\tau)\right],$$

(8)

$$\frac{\partial r}{\partial t} = \frac{c}{eBr}\frac{\partial p_\theta}{\partial t} \equiv -\frac{c}{eBr}\frac{\partial H}{\partial\theta} = \frac{c}{Br}[A_i(r)m_i\cos(m_i\theta)\delta(t)$$

$$- A_s(r)m_s\cos(m_s\theta)\delta(t-\tau)],$$

(9)

where $\omega_E(r) \equiv -c/Br\,\partial\phi_o/\partial r$ is the 2D $\mathbf{E} \times \mathbf{B}$ rotation rate, and we use $p_\theta = (eB/2c)r^2$ to express the canonically conjugate variables (θ, p_θ) as (θ, r^2). Integrating the equations of motion from $t=0$ to a time $t<\tau$, before the second wall excitation, gives

$$\theta = \theta_o + \omega_E(r)t + \delta\theta_i(\theta_o), \quad 0 < t < \tau$$

(10)

$$r^2 = r_o^2 + A_i(r)m_i\frac{2c}{B}\cos(m_i\theta_o), \quad 0 < t < \tau,$$

(11)

where $\delta\theta_i \equiv c/Br\,\partial A_i/\partial r\sin(m_i\theta_o)$ is the impulsive θ drift from the radial electric field of the initial excitation. These θ kicks are ignored in the remaining theory because they are not multiplied by t, so they do not accumulate with time.

Integrating Eqs. (8) and (9) from $t=\tau$ to a time $t>\tau$, after the second wall excitation, i.e., when the echo appears, gives

$$\theta = \theta(\tau) + \omega_E[r(\tau^+)](t-\tau), \quad t > \tau$$

(12)

$$r^2 = r_o^2 + A_i(r)m_i\frac{2c}{B}\cos(m_i\theta_o)$$

$$- A_s(r)m_s\frac{2c}{B}\cos[m_s\theta(\tau)] \quad t > \tau,$$

(13)

where $t=\tau^+$ is the time immediately after the second excitation. The radial displacements caused by the second wall excitation are given by Eq. (13). Particles displaced to a new radial position $r(\tau^+)$ rotate at the new rate $\omega_E[r(\tau^+)]$, enabling unmixing.

Using Eqs. (10) and (11), we evaluate $\theta(\tau)$ as

$$\theta(\tau) = \theta_o + \omega_E \left[r_o + \frac{c}{Br} m_i A_i(r) \cos(m_i \theta_o) \right] \tau$$

$$\simeq \theta_o + \omega_E(r_o)\tau + \frac{c}{Br} \left. \frac{\partial \omega_E}{\partial r} \right|_{r_o} A_i(r) m_i \cos(m_i \theta_o)\tau, \tag{14}$$

where ω_E is Taylor expanded in the last line. Similarly, the term $\omega_E[r(\tau^+)]$ in Eq. (12) is Taylor expanded. The particle θ trajectories of Eq. (12) are then

$$\theta(r_o, \theta_o, t) = \theta_o + \omega_E(r_o)t + \frac{c}{Br} \left. \frac{\partial \omega_E}{\partial r} \right|_{r_o} A_i(r) m_i \cos(m_i \theta_o)t$$

$$- (t - \tau)\frac{c}{Br} \left. \frac{\partial \omega_E}{\partial r} \right|_{r_o} A_s(r) m_s$$

$$\times \cos \left[m_s \theta_o + m_s \omega_E(r_o)\tau \right.$$

$$\left. + \frac{c}{Br} \left. \frac{\partial \omega_E}{\partial r} \right|_{r_o} A_i(r) m_i m_s \cos(m_i \theta_o)\tau \right]. \tag{15}$$

We make use of the exponential expansion

$$e^{-ia \cos x} = \sum_l (-i)^l J_l(a) e^{-ilx}, \tag{16}$$

where J_l is the Bessel function of the first kind of order l, and find that the electric field at the wall vanishes unless $m = qm_s - pm_i$. Here, p and q are the harmonic orders of the initial and second excitations, respectively, similar to l in Eq. (16).

For the lowest harmonic numbers $p = q = 1$, the echo mode number is predicted to be

$$m_e = m_s - m_i. \tag{17}$$

Experiments with a variety of (m_i, m_s) show $m_e = m_s - m_i$ and no echo is seen if $m_i > m_s$.

Furthermore, we use the Bessel function identity

$$J_p(c - d) = \sum_s J_{p+s}(c) J_s(d), \tag{18}$$

and find that the electric field at the wall, for $t > \tau$, is given by

$$E_w(t) = e \int_0^{R_w} r\, dr\, n_o(r) g_m(r|r') \exp\left[-im_e \omega_E(r) \right.$$

$$\times \left(t - \tau \frac{m_s}{m_e} \right) J_1 \left[\frac{c}{Br} \frac{\partial \omega_E}{\partial r} A_i(r) m_i m_e \right.$$

$$\left. \times \left(t - \tau \frac{m_s}{m_e} \right) \right] J_1 \left[\frac{c}{Br} \frac{\partial \omega_E}{\partial r} A_s(r) m_s m_e (t - \tau) \right], \tag{19}$$

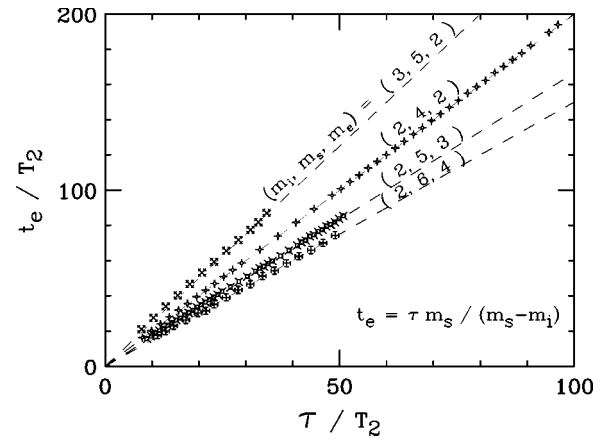where we have dropped the subscript on r for notational convenience.

FIG. 6. Echo appearance time t_e vs the second wave launch time τ, both normalized to the $m = 2$ wave period T_2, using various mode numbers.

A. Time of echo appearance

Equation (19) predicts the time of the echo appearance, which is obtained by setting the phase-mixing terms to zero. In the experiments, phase mixing is the spiral wind-up of the density perturbation, creating radial ripples of δn. The unique time at which the ripples vanish is found by setting the r-dependent terms in the exponential argument to zero, yielding the echo appearance time

$$t_e = \tau \frac{m_s}{m_s - m_i}. \tag{20}$$

We measure the echo appearance time t_e with an automated fit to the wall signal, using a symmetric growing/damping sine wave centered at t_e. The sine wave frequency is at the well-defined mode frequency, which does not even enter the theory. Figure 6 shows the measured t_e versus the second wave launch time τ, both normalized to the $m = 2$ wave period T_2. The dashed lines are the theory predictions, and the initial, second, and echo mode numbers are shown in parentheses. The case with $m_i = 2$ and $m_s = 4$ has the largest data range due to the large signal-to-noise ratio of the measured echo amplitude.

To further compare the collisionless theory with experiments, we evaluate Eq. (19) near the echo appearance time t_e, and write the "no collision" theory prediction for the peak echo wall signal as

$$S_e^{nc} \equiv GE_w(t \approx t_e) = V_i \int_0^{R_w} dr\, \alpha(r) J_1[\beta(r) V_s \tau], \tag{21}$$

where $\alpha(r)$ and $\beta(r)$ are given by

$$\alpha(r) \equiv Ga_i \Delta t_i \epsilon \frac{ecm_i m_e}{2BR_w} \left(\frac{r}{R_w} \right)^{m_i + m_e} n_o(r) \frac{\partial \omega_E}{\partial r}, \tag{22}$$

$$\beta(r) \equiv a_s \Delta t_s m_i m_s \frac{c}{Br} \left(\frac{r}{R_w} \right)^{m_s} \frac{\partial \omega_E}{\partial r}. \tag{23}$$

The gain is given by $G \equiv (A/C)\widetilde{G}$, where A is the area and C is the capacitance of the detection sectors, and where $\widetilde{G}$ is the amplifier gain. The small quantity ϵ represents the difference

between the theoretical echo appearance time t_e and the measurement time. This measurement time is defined as the time of the maximal echo wall signal, and is typically within 1 or 2 plasma rotation periods of the theoretical t_e.

Equation (21) follows from Eq. (19) because at $t \approx t_e$, the Bessel function argument in Eq. (19) containing the *initial* perturbation amplitude is extremely small, and $J_1(x) \approx x/2$ for small x. The Bessel function argument which contains the *second* perturbation amplitude is large at the time of the echo appearance, so this Bessel function is not expanded. Theoretically, at $t = t_e$, the echo wall signal is zero, since $J_1(0) = 0$.

V. COLLISIONAL IRREVERSIBILITY OF END-FIELD θ DRIFTS

In this section, we evaluate a second-order theory that describes collisional scattering between v_z velocities, giving irreversible "θ smearing." θ motion outside the 2D perspective arises from the radial component of the confinement fields, which create $\mathbf{E} \times \mathbf{B}$ drifts in the θ direction.[13] These θ steps depend on the particle's end-residence time, and hence on the particle's z velocity v_z, so one must consider $\omega_E(r, v_z)$. In the absence of collisions or other randomizing effects, each particle remains in its original velocity class, which executes its own spiral wind-up (and unwinding). Thus, the spiral wind-up due to $\omega_E(r)$ and the wind-up due to $\omega_E(v_z)$ have similar phase-mixing effects, and the v_z-dependent θ steps alone do not destroy the echo.

Collisions, however, cause irreversible velocity mixing. Particles scattered into a new velocity class change their bounce-averaged rotation rate $\omega_E(r, v_z)$, which degrades the coherence of the spiral "unwinding," and limits the maximal echo lifetime.

A. Collisional theory

The Boltzmann equation is used to model collisions acting on the particle distribution function $f(r, v_z, t)$,

$$\frac{\partial f}{\partial t} + [f, H'] = \nu \bar{v}^2 \frac{\partial^2 f}{\partial v_z^2}, \tag{24}$$

where ν represents the electron-electron parallel scattering rate $\nu_\parallel$,[15] given by

$$\nu_\parallel \equiv 2.8 \sqrt{\pi} n \bar{v} b^2 \ln(r_L/b). \tag{25}$$

Here, $r_L \equiv \bar{v}/\Omega_c$ is the cyclotron radius and $b \equiv e^2/T$ is the distance of closest approach for thermal electrons.

The Hamiltonian H' used here includes z dynamics, and is given by

$$H' = \frac{p_z^2}{2M} - e\phi_o(r, z) + \delta H'. \tag{26}$$

The perturbed Hamiltonian $\delta H'$ neglects collective effects, similar to Eq. (7), and models the impulsively applied wall excitations:

$$\delta H' = eA_i(r)e^{im_i\theta}\delta(t) + eA_s(r)e^{-im_s\theta}\delta(t - \tau). \tag{27}$$

For $t < \tau$, the first-order solution from the initial excitation only is

$$\delta f_i^{(1)} = -im_i A_i \frac{c}{eBr} \frac{\partial f_M}{\partial r} \cdot \exp\left[-im_i\theta + im_i\omega_E(r)t \right.$$
$$\left. - \frac{im_i v_z^2}{\Omega_c Lr} \frac{\partial L}{\partial r} t - \nu \frac{4}{3} \frac{m_i^2 v_z^2 \bar{v}^2}{\Omega_c^2 L^2 r^2} \left(\frac{\partial L}{\partial r}\right)^2 t^3 \right]. \tag{28}$$

The $\omega_E(v_z)$ effect is seen in the third term in the exponential argument. Here, $\partial f_M/\partial r$ is the radial derivative of the unperturbed distribution function, which is assumed to be Maxwellian, and $\partial L/\partial r$ represents the curvature in the ends of the plasma. In obtaining Eq. (28), we have made the approximation $\partial^2/\partial v_z^2 \delta f \simeq 1/\delta f(\partial/\partial v_z \delta f)^2$. The rather strange t^3 scaling of the collisional term in the exponent comes from the collision operator $\nu \bar{v}^2(\partial^2/\partial v_z^2)$ acting on δf, which has the v_z-dependent θ-smearing effect in $\omega_E(r, v_z)$. This brings down t^2 and the integral $\nu \bar{v} \int_0^t dt'(\partial^2 \delta f/\partial v_z^2)$ then yields t^3.

Solving the Boltzmann equation to second order, and keeping only terms containing the first power of ν, we find that the perturbed distribution function at $t > \tau$ is given by

$$\delta f^{(2)}(t) = im_i^2 m_s \left(\frac{c}{Br}\right)^2 \frac{\partial \omega_E}{\partial r} \frac{\partial f_M}{\partial r} A_i A_s \tau$$
$$\times \exp\left[im_e\theta - i\omega_E(r, v_z)m_e\left(t - \frac{\tau m_s}{m_e}\right) \right] \cdot$$
$$\times \exp\left\{ -\nu \frac{4v_z^2 \bar{v}^2}{\Omega_c^2 L^2 r^2}\left(\frac{\partial L}{\partial r}\right)^2 \left[\frac{m_i^2 \tau^3}{3} \right.\right.$$
$$\left.\left. + \frac{m_e^2(t - \tau)^3}{3} + m_i^2 \tau^2(t - \tau) - m_i m_e \tau(t - \tau)^2 \right] \right\}. \tag{29}$$

Again, the time of the echo appearance t_e is obtained by setting the r-dependent (phase mixing) terms in the first exponential argument equal to zero.

At time $t = t_e \equiv \tau m_s/m_e$, the second-order collisional solution for the peak echo amplitude is

$$\delta f^{(2)}(t_e) = im_i^2 m_s \left(\frac{c}{Br}\right)^2 \frac{\partial \omega_E}{\partial r} \frac{\partial f_M}{\partial r} A_i A_s \tau$$
$$\times \exp(im_e\theta)\exp[-\gamma^3(\nu, r, \varepsilon_z)\tau^3], \tag{30}$$

where the collisional damping term is given by

$$\gamma^3(\nu, r, \varepsilon_z) \equiv \nu \varepsilon_z T \left(\frac{c}{eBr}\right)^2 \left(\frac{1}{L}\frac{\partial L}{\partial r}\right)^2 \frac{8}{3}\frac{m_i^2 m_s}{m_e}. \tag{31}$$

Here, $\varepsilon_z \equiv Mv_z^2/2$ is the electron kinetic energy, and the plasma length $L(r, \varepsilon_z)$ is defined by the electron end reflection at $L/2$:

$$e\phi(r, \pm L/2) - e\phi(r, 0) = \varepsilon_z. \tag{32}$$

Finally, we combine the collisionless result of Eq. (21) with the collisional result of Eq. (29), and find that the peak echo wall signal, near the echo appearance time, is given by
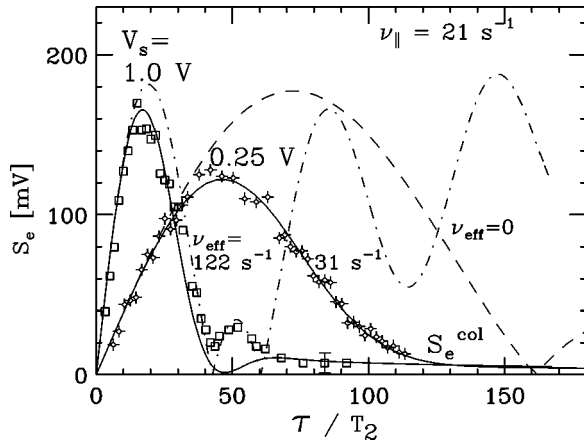
FIG. 7. Measured peak echo wall signal S_e vs the second wave launch time τ for two different second excitation voltages V_s. The solid lines show fits from numerically integrating the collisional theory expression of Eq. (33). The dashed and dot-dashed lines have $\nu_{eff}=0$.

$$S_e^{col} = \alpha' V_i \int_0^{R_w} dr\, r^{m_i+m_e+1} \frac{\partial \omega_E}{\partial r} \frac{\partial n_o}{\partial r} J_1\left(\beta' r^{m_s-1} \frac{\partial \omega_E}{\partial r} V_s \tau\right)$$

$$\times \frac{1}{2\sqrt{\pi T}} \int_0^\infty \frac{d\varepsilon_z}{\sqrt{\varepsilon_z}} \exp[-\varepsilon_z/T - \gamma^3(\nu_{eff},r,\varepsilon_z)\tau^3],$$

$$(33)$$

where α' and β' are the coefficients of α and β in Eqs. (22) and (23), and are given by

$$\alpha' \equiv Ga_i \Delta t_i \epsilon \frac{ecm_i m_e}{2BR_w^{m_i+m_e+1}},$$

$$(34)$$

$$\beta' \equiv a_s \Delta t_s m_i m_s \frac{c}{BR_w^{m_s}}.$$

$$(35)$$

The $1/\sqrt{\varepsilon_z}$ term arises from changing a velocity integral $\delta n = \int dv\, \delta f$ to an energy integral $\delta n = \int d\varepsilon_z \delta f / \sqrt{2M\varepsilon_z}$. In order to compare with experiments, the collision rate ν in the collisional damping term γ^3 has been written in terms of an effective collision rate ν_{eff}:

$$\nu \equiv \nu_{eff} \frac{n(r)}{n(0)} (\varepsilon_z/T)^{-1}.$$

$$(36)$$

B. Comparison with experiments

We numerically evaluate the double integral in Eq. (33). A 2D Poisson solver[16] is used to calculate the local density $n(r,z)$ and potential $\phi(r,z)$ from the measured z-integrated density from a CCD image. In obtaining the solution, local thermal equilibrium is presumed at every r and z. The plasma length $L(r,\varepsilon_z)$ is then calculated from Eq. (32), and the plasma rotation frequency is calculated from $\omega_E(r) \equiv -c/Br\partial\phi(r)/\partial r$, at $z=0$.

We obtain an effective electron-electron collision rate ν_{eff} by fitting S_e^{col} of Eq. (33) to data sets of the measured peak echo wall signal S_e versus τ, with ν_{eff}, α', and β' as fitting parameters. The solid lines of Fig. 7 are examples of such a fit using two different excitation voltages V_s; all other
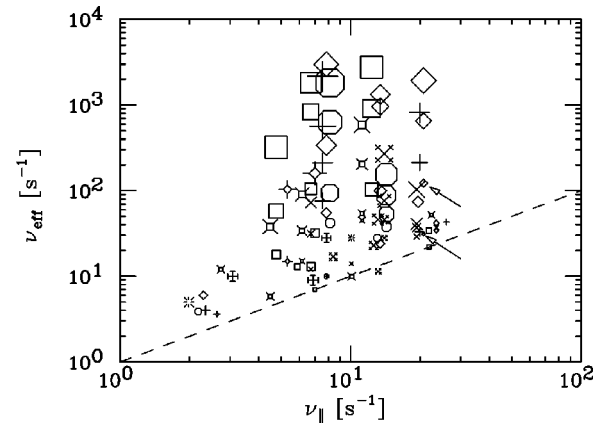

FIG. 8. Echo data showing the measured ν_{eff} vs actual electron-electron collision rate $\nu_\parallel$. The size of the data symbols represents the strength of the second wave perturbation.

parameters are held constant. For the weak second wave excitation of $V_s=0.25$ V, the fit yields $\nu_{eff}=31$ sec^{-1}, which is fairly close to the actual electron-electron scattering rate of $\nu_\parallel=21$ sec^{-1}. Thus, the decrease in S_e represents collisional irreversibility. The simple collisionless theory ($\nu_{eff}=0$) is also shown dashed and dot dashed, using the same α' and β' as the solid lines.

At the larger second excitation of $V_s=1.0$ V, the decrease in S_e at $\tau \approx 20T_2$ represents the nonlinear saturation effect described by the Bessel function in Eqs. (21) and (33). Here, the fit yields $\nu_{eff}=122$ sec^{-1}, which does not represent a measure of collisionality, but rather represents the absence of the late-time echo recurrence at $\tau \approx 85T_2$ (and $\tau \approx 150T_2$).

Figure 8 summarizes the comparison between the collisional theory and echo data. The vertical axis is the experimentally determined ν_{eff}, obtained from fits to 65 data sets such as Fig. 7. The horizontal axis is the actual electron-electron collision rate $\nu_\parallel$ for the specific plasma parameters, given by Eq. (25). The measured ν_{eff} is always greater than that expected from $\nu_\parallel$ alone.

In Fig. 8, the strength of the applied wall voltage V_s used to excited the second wave is represented (logarithmically) by the size of the data symbol, with larger symbols corresponding to larger second excitation strengths. At a given value of $\nu_\parallel$, identical symbols of different sizes correspond to identical plasma parameters, but with different values of the second wave excitation strength. The strength of V_s is varied over a factor of 50 in the data plotted here. The arrows identify the data points corresponding to Fig. 7.

Figure 8 shows that the echo lifetime is limited by collisional irreversibility of end-field θ smearing when the second wave excitation is sufficiently small. At large second wave amplitudes, a different (unknown) effect destroys the echo as effectively as collisions enhanced by $100\times$. These large values of ν_{eff} represent the absence of echo recurrence at large values of $V_s\tau$.

Note that the large variations in ν_{eff} translate into much smaller variations in the time of echo destruction, because of the τ^3 scaling in the collisional exponential decay argument in Eq. (33). Thus, a factor of 100 enhancement in ν_{eff} gives only a $4.6\times$ reduction in the echo viability time.
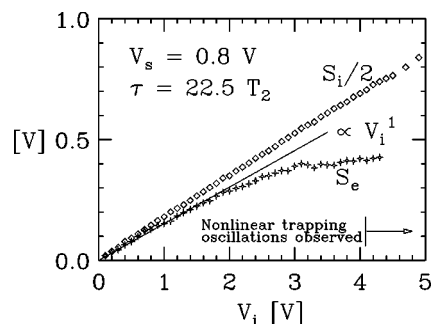
FIG. 9. The peak initial wave and echo wave wall signals, S_i and S_e, respectively, vs the initial wave excitation voltage V_i. The solid line is the theory prediction $S_e \propto V_i$.

VI. LARGE AMPLITUDE EFFECT

The absence of echo recurrence at large second wave amplitudes may be due to collective plasma effects, including particle trapping by the wave potential.[17] This trapping effect causes particles to deviate from ballistic, free-streaming orbits, and limits phase unmixing.

Figure 9 shows that the peak measured echo signal S_e is linearly proportional to the initial excitation voltage V_i, as predicted by Eq. (33), until $V_i \gtrsim 2$ V. As the excitation amplitude is increased, nonlinear bouncing oscillations are observed in the wall signal of the initial wave damping, indicating that particles are trapped by the initial wave potential.

Presumably, large second wave excitations also cause particle trapping by the second wave potential, although sector geometry prevents direct observation of trapping oscillations. This particle trapping may be responsible for the observed increase in ν_{eff} at large V_s in Fig. 8.

VII. SUMMARY

We have observed fluid echoes in a pure electron plasma, explicitly demonstrating the reversible nature of spatial Landau damping. The phase mixing and unmixing associated with wave damping and echo generation are imaged directly, and the echo mode number, appearance time, and saturation effect agree with a simple ballistic theory. The pure electron plasma behaves like an ideal 2D fluid, despite 3D end effects that make ω_E dependent on an electron's z velocity. Different velocity classes separately phase mix and unmix, surprisingly forming the same echo. At late times the echo is degraded, and collisional scattering between velocity classes gives a fundamental limit to the echo lifetime. In addition, large amplitude effects degrade the echo up to $5\times$ faster than collisions.

[1]N. A. Kurnit, J. D. Abella, and S. K. Hartman, Phys. Rev. Lett. **13**, 567 (1964).
[2]E. L. Hahn, Phys. Rev. **80**, 580 (1950).
[3]R. W. Gould, Am. J. Phys. **37**, 585 (1969).
[4]T. M. O'Neil and R. W. Gould, Phys. Fluids **11**, 134 (1968).
[5]J. H. Malmberg, C. B. Wharton, R. W. Gould, and T. M. O'Neil, Phys. Fluids **11**, 1147 (1968).
[6]R. W. Gould, Phys. Plasmas **2**, 2151 (1995).
[7]A. E. Lifshits, Sov. Phys. Dokl. **34**, 783 (1989).
[8]J. Vanneste, P. J. Morrison, and T. Warn, Phys. Fluids **10**, 1398 (1998); D. A. Bachman, Ph.D. thesis, California Institute of Technology, 1998.
[9]C. F. Driscoll and K. S. Fine, Phys. Fluids B **2**, 1359 (1990).
[10]H. Lamb, *Hydrodynamics*, 6th ed. (Dover, New York, 1932), Secs. 158 and 159; L. Kelvin, Philos. Mag. **10**, 155 (1880).
[11]R. H. Levy, Phys. Fluids **8**, 1288 (1965); R. J. Briggs, J. D. Daugherty, and R. H. Levy, *ibid.* **13**, 421 (1970).
[12]D. A. Schecter, D. H. Dubin, A. C. Cass, C. F. Driscoll, I. M. Lansky, and T. M. O'Neil, Phys. Fluids **12**, 2397 (2000).
[13]A. J. Peurrung and J. Fajans, Phys. Fluids A **5**, 4295 (1993); D. H. Dubin and T. M. O'Neil, Phys. Plasmas **5**, 1305 (1998).
[14]D. A. Schecter, Ph.D. thesis, University of California at San Diego, 1999.
[15]S. Ichimaru, *Basic Principles of Plasma Physics* (W.A. Benjamin, Reading, 1973), p. 244.
[16]See National Technical Information Service Document No. DE97053509 [direct numerical solution of Poisson's equation in cylindrical (r, θ) coordinates]. Copies may be ordered from the National Technical Information Service, Springfield, VA 22161.
[17]N. S. Pillai and R. W. Gould, Phys. Rev. Lett. **73**, 2849 (1994).